Spectrochimica Acta Part B 87 (2013) 43–50

Contents lists available at ScienceDirect

Spectrochimica Acta Part B

journal homepage: www.elsevier.com/locate/sab

Comparison of optical emission from nanosecond and femtosecond laser produced plasma in atmosphere and vacuum conditions

J.R. Freeman *, S.S. Harilal, P.K. Diwakar, B. Verhoff, A. Hassanein

Center for Materials Under eXtreme Environment, School of Nuclear Engineering, Purdue University, 500 Central Drive, West Lafayette, IN 47907, USA

ARTICLE INFO

Article history:
Received 30 November 2012
Accepted 12 May 2013
Available online 18 May 2013

Keywords:
Optical emission spectroscopy
Laser-induced breakdown spectroscopy
Laser-produced plasma
Plasma dynamics
Femtosecond laser ablation

ABSTRACT

In this study we examine the emission from brass plasma produced by ns and fs laser ablation under both vacuum and atmosphere environments using identical laser fluences in order to better understand the differences in emission features and plasma dynamics. Optical emission spectra show increased continuum and emission from lower-charged ions for ns laser-produced plasma (LPP), while fs plasma emission spectra show emission primarily from excited neutral species with negligible continuum. Plasma excitation temperature and electron density as a function of time show similar trends for both lasers, though fs LPP expansion appears to be approximately two times faster than ns LPP expansion for the conditions studied. Confinement by the ambient gas is shown to significantly enhance and maintain plasma temperature and density and hence, emission, at later times. ICCD images of plasma expansion showed a broader angular distribution for ns LPP, but narrower angular distribution for fs LPP. Images also confirm the significant effect that the ambient environment has in confining plume expansion.

1. Introduction

The field of laser ablation and analysis of subsequent light emission has been growing since the development of the laser in the 1960s. One of the well-known applications of laser ablation is laser-induced breakdown spectroscopy (LIBS). LIBS is a technique commonly used to identify constituents of an unknown sample by ablating a small amount of the sample and studying the resultant optical emission [1–3]. LIBS has been applied to many fields as an analytical instrument, such as deep sea [4], extraterrestrial [5], artwork [6], explosive residue [7], and thin film [8] analysis. While LIBS experiments are primarily performed in an ambient atmosphere environment, the impact of low-pressure environments is also important for certain fields such as nuclear fusion reactor analysis [9] and space exploration [5,10].

As with all laser ablation, the properties of the LIBS plasma and its emission are strongly dependent on laser parameters such as energy, pulse length, and wavelength. Traditionally, LIBS systems have employed nanosecond (ns) laser systems, but with the recent developments in femtosecond (fs) laser systems, much attention has been turned to development of fs LIBS systems, as they offer greatly reduced thermal damage and heat affected zone (HAZ) due to negligible heat conduction and hydrodynamic motion during the laser pulse duration [11].

The differences between ns and fs laser ablation mechanisms are drastic due to the significant differences in laser pulse length. Whereas ionization, sample heating, and vaporization all occur during the laser pulse in ns laser ablation, fs laser pulses are too short that these phenomena do not occur until the end of the laser pulse. Because the laser pulse is shorter than the electron relaxation time in the lattice, all laser energy is deposited onto the target before ablation begins, on the order of picoseconds later. During the fs laser pulse, seed free electrons are produced through strong-electric-field, avalanche, and multiphoton ionization [12] and once critical electron density is reached, laser photons are absorbed primarily though inverse bremsstrahlung (IB) absorption. This ionization of lattice atoms results in wide bandgap materials exhibiting metallic properties, as valence electrons are rapidly excited into the conduction band. The energetic free electrons then produce additional free electrons through a series of impact ionization collisions, referred to as avalanche ionization [13,14]. At laser energies of the order of 10^{13} W/cm^2 and higher, multiphoton ionization becomes the dominant ionization process creating seed free electrons [15]. Ionization occurs at time scales shorter than that needed for electrons to transfer energy to the lattice and all absorbed laser energy is concentrated within the electrons near the surface of the sample. The two competing mechanisms attributed to material ablation by fs lasers are the Coulomb explosion and thermal vaporization [16,17]. Lattice melting and ablation occur on the order of several picoseconds after the laser pulse [18]. During Coulomb explosion, energetic free electrons are ejected from the surface leaving highly charged ions in the bulk material. These highly charged ions repel each other and are pulled by

* Corresponding author.
E-mail addresses: freemaj@purdue.edu (J.R. Freeman), sharilal@purdue.edu (S.S. Harilal), pdiwakar@purdue.edu (P.K. Diwakar), bverhoff@purdue.edu (B. Verhoff), hassanein@purdue.edu (A. Hassanein).

0584-8547/$ – see front matter © 2013 Elsevier B.V. All rights reserved.
http://dx.doi.org/10.1016/j.sab.2013.05.011

the oppositely charged electrons out of the bulk material resulting in an explosion of highly ionized plasma. This ejection of excited, highly ionized species is responsible for emission in the extreme-UV and X-ray regions. At sufficiently high laser intensities, thermal vaporization is the major mechanism for fs laser ablation. To summarize, fs laser ablation deposits all laser energy directly onto the target surface creating highly-ionized species and subsequent thermal vaporization of the target, while most of the laser energy in ns laser ablation is deposited on the expanding plasma plume, contributing towards additional heating and ionization of plume species. From these different ablation schemes, plume dynamics can be expected to be significantly different between ns and fs laser ablation and their differences should be investigated to better understand and optimize the use of these lasers for various applications.

The kinematic and radiative properties of plasmas are strongly dependent on plasma temperature and density, making these two plasma parameters crucial in the optimization of plasma sources. Though these parameters can be determined using a number of experimental techniques [19–22], one of the most commonly used and non-intrusive methods is that of optical emission spectroscopy, where temperature and density estimates can be made using spectral intensities and line widths, respectively. We recently reported the evolution of temperature and density of ns and fs LIBS plumes in vacuum using spectroscopic means [23]. In this article, we extend that work by comparing the features of ns and fs LIBS plumes both in vacuum and atmosphere environments along with important analytical merits.

We examine the dynamics of ns and fs LIBS plumes in both atmosphere and vacuum conditions using optical imaging and spectroscopic techniques. Images of the expanding plasma were obtained using an ICCD to demonstrate the effect of the ambient environment on plasma expansion and identify key differences between fs and ns LPP plume expansion. Emission spectra from both lasers in both pressure environments were studied at different delays after the laser pulse and particular emission features specific to each have been identified. Excitation temperature and density of the plumes were then estimated using Boltzmann plot and Stark broadening techniques, respectively, allowing us to better understand the differences in the dynamic properties from different pulse duration lasers and in different pressure environments. A systematic comparison of analytical performance (signal-to-noise and signal-to-background) is also given for both ns and fs LPPs in vacuum and ambient air atmosphere.

2. Experimental setup

The schematic of the experimental setup is given in Fig. 1. Experiments were conducted inside a chamber evacuated to a pressure ~ 10^{-5} Torr for obtaining LPP vacuum data and vented using ambient air at atmospheric pressure for recording LPP atmosphere data. A brass target consisting of roughly 70% copper and 30% zinc was used for plasma creation. Plasma creation was accomplished using a Nd:YAG laser (Surelite II, continuum lasers) for ns laser pulses and a Ti–Sapphire laser for fs laser pulses. The ns laser produces 8 ns full width half maximum (FWHM) pulses, measured using a fast photodiode with a rise time of approximately 300 ps, at its fundamental wavelength of 1064 nm. The fs laser uses a mode-locked Ti–Sapphire oscillator (Synergy, Femtolase, Inc.) in conjunction with a chirped pulse amplifier (Amplitude Technology, Inc.) to produce 40 fs laser pulses, measured using an autocorrelator, at a wavelength of 800 nm. The amplifier system for the fs laser includes a pulse stretcher, regenerative amplifier, multi-pass amplifier, and a compressor. Laser energy used for both ns and fs lasers was 6 mJ and a 100 μm spot size was maintained to keep the same laser fluence (76.4 J cm^{-2}) and hence, energy deposited per unit area on the target was the same for both lasers. Laser energies were attenuated using a combination of waveplate and polarizing cube beamsplitter for the ns laser and a waveplate and thin film polarizer beamsplitter placed before the compressor for the fs laser.

To obtain the time-resolved plasma emission spectra, a 0.5 m focal length spectrograph (Acton, SP2500i) equipped with an intensified charge-coupled device offering a minimum gate width of 2 ns (ICCD, Princeton Instruments PI-MAX) was used. A programmable timing generator (PTG) was used to synchronize the ICCD camera with the laser pulse. Accumulation times for spectra were maintained at 10% of the gate delay, providing time-resolved spectra. Collection of plasma emission was done at a position normal to the direction of plasma expansion and was achieved by collimating the light with one lens close to the plasma and using another lens to focus the

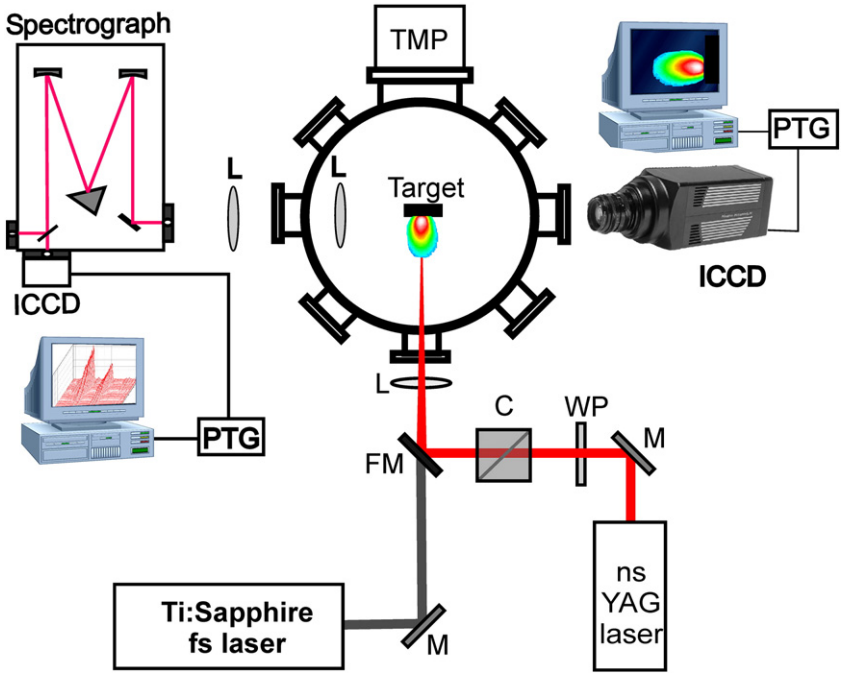

Fig. 1. Schematic of the experimental setup (TMP, turbomolecular pump; PTG, programmable timing generator; L, lens; ICCD, intensified charge-coupled device; FM, flip mirror; M, mirror; C, cube polarizer; WP, waveplate).

light onto the spectrograph slit. A 150 grooves/mm grating was used to record spectra for the plasma excitation temperature calculations in order to obtain a wide wavelength range with a single laser shot, thereby minimizing shot-to-shot emission intensity fluctuations that can arise when stitching several spectra together. Intensity values of the lines of interest were corrected according to the efficiency of the spectrograph system at the chose wavelength. To record spectra for plasma electron density calculations, a grating with 1800 grooves/mm was used to obtain higher spectral resolution. The PTG and ICCD were used without the spectrograph and at an angle normal to plasma expansion to directly capture images of the time-integrated plasma emission.

3. Results and discussion

We used optical emission spectroscopic techniques to characterize plumes generated by ns and fs lasers. Many spectroscopic applications, LIBS in particular, are traditionally performed in atmospheric conditions, but in order to fully understand what happens within the plume, especially at early times in its formation, it is crucial to understand how the plume evolves in a free, vacuum environment. Because of this we characterized ns and fs LPP in both vacuum and atmosphere environments to determine the effect of the ambient gas on plume dynamics. ICCD images were used to visualize plasma expansion of ns and fs LPP and the effect of confinement by an ambient environment. We then compared the emission spectra of ns and fs LPP in vacuum and atmosphere conditions at different delays after the laser pulse to identify differences in the spectra and evolution. Plasma electron density and excitation temperature were then estimated as a function of delay after laser pulse in order to better understand the dynamics occurring within the plasma.

3.1. ICCD imaging of plasma emission and expansion characteristics

Figs. 2 and 3 show ICCD 2 μs time-integrated images of the visible emission from ns and fs LPP, respectively. All intensities have been normalized to the maximum intensity seen from both figures and are displayed on a logarithmic scale. We see a significant difference in expansion of emitting species between ambient atmosphere and vacuum environments. For the case of ns LPP emission (Fig. 2) expansion of the plume with a wider angular distribution is observed. In vacuum, expansion of the emitting species is significant and emission can be seen at distances greater than 10 mm from the target. However in atmosphere conditions, where plume expansion is confined by the ambient gas, expansion of emitting species is limited to a distance of ~2.5 mm from the target, creating a smaller source, which is beneficial for light-collection optics in LIBS systems. Higher emission intensities are seen in the atmosphere case due to confinement, as emission is concentrated in a smaller region.

Expansion dynamics of fs LPP is significantly different from ns LPP. Instead of wide-angle expansion noticed in ns LPP, fs LPP plumes are found to expand with a much stronger forward bias in directions normal to the target surface [23–25], as seen in both atmosphere and vacuum cases in Fig. 3. This is also consistent with our recent results which showed that fs LPP provided narrower angular distribution of ions and evaporated mass in comparison with ns LPPs [25]. The narrow-angle fs LPP expansion may be explained by strong self-generated magnetic fields on the order of tens of Tesla [26–28] that serve to pinch and direct the plasma in the direction normal to the target [29,30]. Like the ns LPP case in vacuum, expansion of emitting species in fs LPP can also be seen at distances greater than 10 mm, while in atmosphere, stronger emission can be seen farther from the target surface in the case of fs LPP due to the pinching and more focused angular spread in the expansion of the plasma. As was true in the ns case, emission intensities are higher in the atmosphere case, as emission is confined in a smaller region. Lower visible emission intensities were observed from the fs LPP than those observed from the ns LPP despite similar laser fluence conditions.

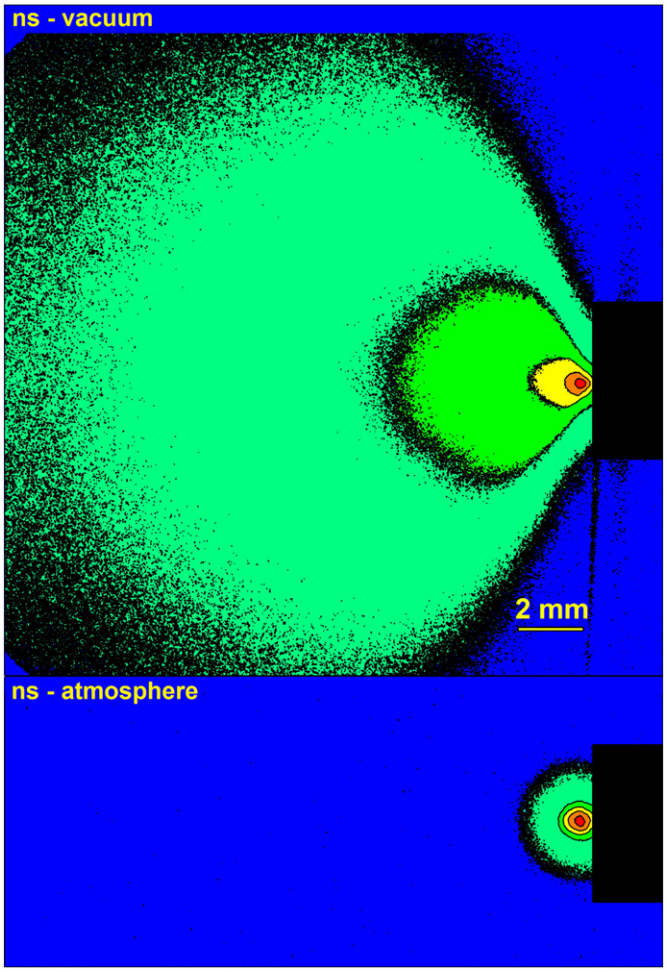

Fig. 2. ICCD time-integrated images of emission from ns LPP in atmosphere and vacuum, displaying effect of confinement by ambient gas. Image intensities are displayed on a logarithmic scale and are normalized to the maximum intensity observed from Figs. 2 and 3.

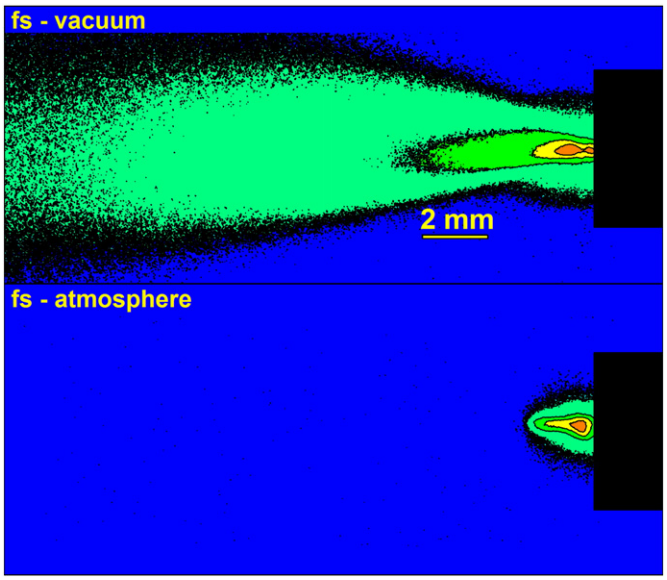

Fig. 3. ICCD time-integrated images of emission from fs LPP in atmosphere and vacuum, displaying effect of confinement by ambient gas. Image intensities are displayed on a logarithmic scale and are normalized to the maximum intensity observed from Figs. 2 and 3.

3.2. Comparison of emission spectra at different delays after the laser pulse

Fig. 4 shows emission spectra from ns and fs LPP in vacuum and atmosphere environments at different times after the laser pulse. Integration times used were 10% of the gate delay after the laser pulse. The ns LPP spectra showed significant continuum especially at times <50 ns, while the continuum emission is greatly reduced in fs LPP spectra. The time-resolved spectral features given in Fig. 4 show the fs LPP spectra are dominated by excited neutrals even at the initial times while the ns LPP spectra are dominated by ions along with intense continuum. In the case of ns LPP, the beginning of the laser pulse deposits energy onto the target, ablating and creating plasma. Much of the rest of the ns laser pulse is then deposited onto the expanding plasma, directly heating and ionizing the plume resulting intense continuum along with ionic line emission at the earliest times. Though similar laser fluences are used for generating ns and fs LPPs in the present experiment, the power densities at the target is significantly higher for fs LPP: ~ 1×10^{10} W/cm^2 and ~ 1.2×10^{15} W/cm^2 for ns and fs LPPs, respectively. The Coulomb explosion and thermal vaporization [16,17] are two competing mechanisms responsible for fs laser material ablation. The Coulomb explosion generally occurs for near-ablation threshold energies, whereas thermal vaporization dominates for energies above threshold. At sufficiently high laser intensities, the Coulomb explosion is followed by thermal vaporization of the bulk material several picoseconds later [31]. Thermal vaporization produces a mostly atomic plume, as temperatures of the emitted species are near to the vaporization point of the bulk and such species were far enough below the surface that ionization by the laser pulse is minimized. Hence the thermal vaporization from the target produces mostly neutral species at temperatures close to the vaporization point [16,17,31] that can be expected to emit in the visible region. As demonstrated in the spectra for fs LPP, we see primarily neutral emission with little to no ionic emission in both vacuum and atmosphere cases. The fs LPP emission spectra also display very similar features, regardless of vacuum or atmosphere environments, though in vacuum the peak emission intensities occur earlier and decay quickly due to free, unimpeded expansion of the plasma plume. However, in atmosphere the peak emission intensities occur at a later time. This is caused by increased excitation and slower expansion within the plasma plume due to confinement in the ambient environment.

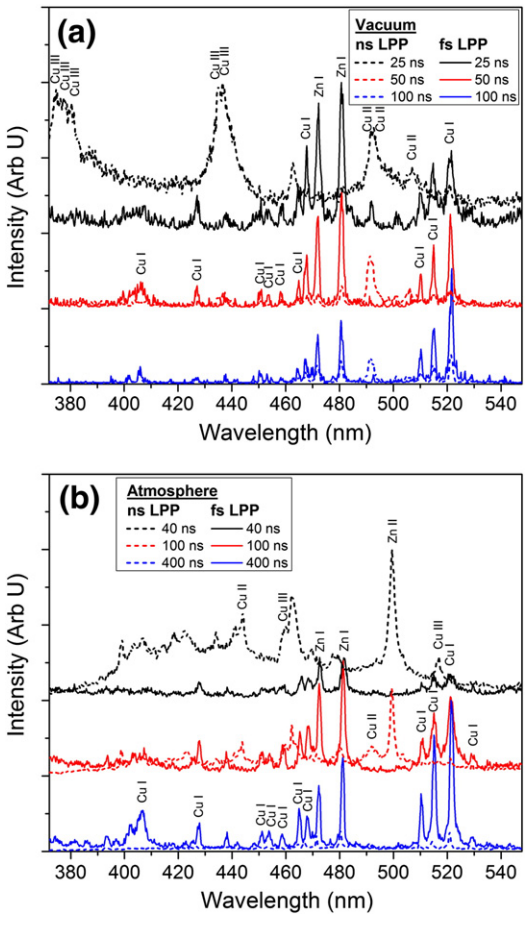

Fig. 4. Spectral emission from ns and fs LPP in vacuum (a) and atmosphere (b) at different gate delays, collected 1 mm from the target. Spectra have been scaled upwards for clearer viewing. Each set of three ns or fs LPP spectra were normalized to the peak intensity of that individual set for comparison of intensity fluctuations at different gate delays. Atomic species identification provided for spectral lines.

In the case of ns LPP emission, strong continuum emission can be seen at early times. The strong peaks seen in these spectra are attributed to ionic emission and are not clearly visible in the fs LPP spectra, as previously discussed. Also, neutral emission peaks that are seen clearly in the fs LPP spectra are not evident at early times in the ns LPP spectra, requiring longer delays to appear and are at lower intensities compared to the ionic emission at early times. This can be attributed to higher populations of lower-charged ions emitting in the visible region compared to neutral atoms, though once these ion populations decrease due to recombination processes in the plume at later times, emission from neutral species dominates. The effect of confinement of the ambient air for ns LPP emission is similar to that for fs LPP emission. Spectral line emission persists longer in the atmosphere case. It is important to note that in both vacuum and atmosphere cases, ns LPP emission exhibits stronger persistence than fs LPP emission, with spectral features present at times much longer than those seen for fs LPP.

Signal-to-noise (S/N) and signal-to-background (S/B) have been calculated using the peak intensity, I_{Max}, of the 481.05 nm Zn I line, the averaged background intensity, $I_{Background}$, on the higher and lower wavelength sides of the line, and the standard deviation, $\sigma_{Background}$, of the background intensities on the higher and lower wavelength sides of the line according to the following equations:

$$\frac{S}{N} = \frac{I_{Max} - I_{Background}}{\sigma_{Background}} \quad (1)$$

$$\frac{S}{B} = \frac{I_{Max}}{I_{Background}} \quad (2)$$

Values found in Table 1 were obtained using time-resolved spectral measurements of ns and fs LPPs both in vacuum and atmospheric pressure. We see that the spectral collection time after the laser pulse is a very important parameter in improving S/N and S/B, as the limit of detection of a system is directly related to these ratios. In vacuum and at earlier times, the fs LPP provides improved S/N and S/B ratios. However, both S/N and S/B ratios are found to improve with respect to time when the plasmas are evolving in the presence of 1 atmosphere air. At early times after the laser pulse S/N and S/B ratios are poor for ns LPP due to strong continuum emission dominating over the neutral line emission, especially in atmosphere as free electrons are confined within the plume. In vacuum these values peak early in the plasma evolution as free expansion results in reduced continuum emission, while in atmosphere these values continue to increase at later times because of confinement of the plume, resulting in electron-ion recombination and hence, significantly reduced continuum emission and increased neutral emission. It should be noted that the S/N and S/B ratios given here are measured from the spectral details collected at 1 mm from the target surface and hence it is not necessary to be representative of entire plume. Spatially integrated spectral measurements are required for estimating S/N and S/B ratio of fs and ns LIBS plumes.

Table 1
Time-resolved S/N and S/B ratios calculated at different times after the laser pulse using Zn I line at 481.05 nm. Empty values are the result of unresolved spectral lines due to strong continuum emission and low neutral populations at early times or negligible emission at later times. The spectral features of ns and fs LPPs were collected at 1 mm from the target.

Time (ns)	S/N				S/B			
	ns LPP		fs LPP		ns LPP		fs LPP	
	Vacuum	Atmosphere	Vacuum	Atmosphere	Vacuum	Atmosphere	Vacuum	Atmosphere
50	12.16	–	51.19	14.85	5.27	–	27.08	9.40
100	122.19	4.56	74.17	23.52	31.61	2.94	24.68	18.94
200	210.54	17.15	15.13	46.28	30.28	8.49	1.98	31.81
400	86.55	23.52	15.61	83.78	11.84	13.69	2.06	50.29
1000	–	52.46	–	139.76	–	26.64	–	21.51
2000	–	288.08	–	–	–	25.39	–	–

3.3. Electron density estimates in vacuum and atmosphere environments

Electron density estimates were made based on the Stark broadening effect of spectral lines by charged particles. The electron number density is related to the FWHM of a spectral line, $\Delta\lambda_{1/2}$ [32]. For LPPs, the broadening contribution from ions is expected to be insignificant compared to that from electrons and can be neglected, simplifying the calculation to:

$$\Delta\lambda_{1/2}\,(nm) = 2W\left(\frac{n_e}{10^{16}}\right) \tag{3}$$

In Eq. (3), the electron impact width parameter, W, is a function of plasma temperature and can be found using reference literature [33]. The spectral line shape must also be corrected for instrumental broadening [34].

Fig. 5 shows the time-resolved plasma electron density as a function of time after the laser pulse for ns and fs LPP in vacuum and atmosphere. Integration times used were 10% of the gate delay after the laser pulse. Electron density estimates were performed using the Zn I line at 481.05 nm and Eq. (3). Density estimates using the Stark broadening technique are difficult to obtain at earlier times, especially in the ns case, as strong continuum and ion emission dominate over the neutral species populations that are used to calculate electron density. The dominant mechanism for forming these neutral species is collisional three-body recombination, the rate of which (R_c) is given by [35]:

$$R_c \propto Z^3 \ln\sqrt{Z^2+1}\,T_e^{-9/2} n_e n_i, \tag{4}$$

where Z is the charge state, T_e is the electron temperature, and n_i is the ion density. As seen in Eq. (4), recombination rate is strongly dependent on temperature. When temperatures in the plasma are high, recombination rates, and hence production of neutral species, will be low, but as temperatures decrease through collisions and radiative processes at later times, recombination rates will increase, producing increased populations of neutral species emitting in the visible region that we have used to estimate density and temperature. The low populations and weak emission at very early times contributes to the larger error seen at earlier times in data.

In vacuum both ns and fs plume density decreases rapidly compared to the atmosphere case. This is due to the free expansion in vacuum rather than confinement of the plume by the ambient environment, as expansion, along with recombination of electrons and ions, are the dominant causes of decreasing electron density [23,36,37]. This confinement in atmosphere also causes an increased persistence of the line emission, resulting in higher densities than those seen in vacuum at similar times. It is important to note the difference in time scales in Fig. 5(a) and (b), as the fs plume expansion appears to occur faster, as electron densities at the onset of visible line emission are similar between fs and ns LPP and at later times electron densities in the fs case reach comparable values to those in the ns case in approximately half the time.

3.4. Excitation temperature estimates in vacuum and atmosphere environments

Plasma excitation temperature calculations were performed using the Boltzmann plot method, which estimates temperature based on the intensity ratios of spectral lines. By using the equation [32]:

$$\ln\left(\frac{I_{ki}\lambda}{g_k A_{ki}}\right) = -\frac{1}{k_B T_{ex}} E_j + \ln\left(\frac{hcn_e}{4\pi U(T_{ex})}\right), \tag{5}$$

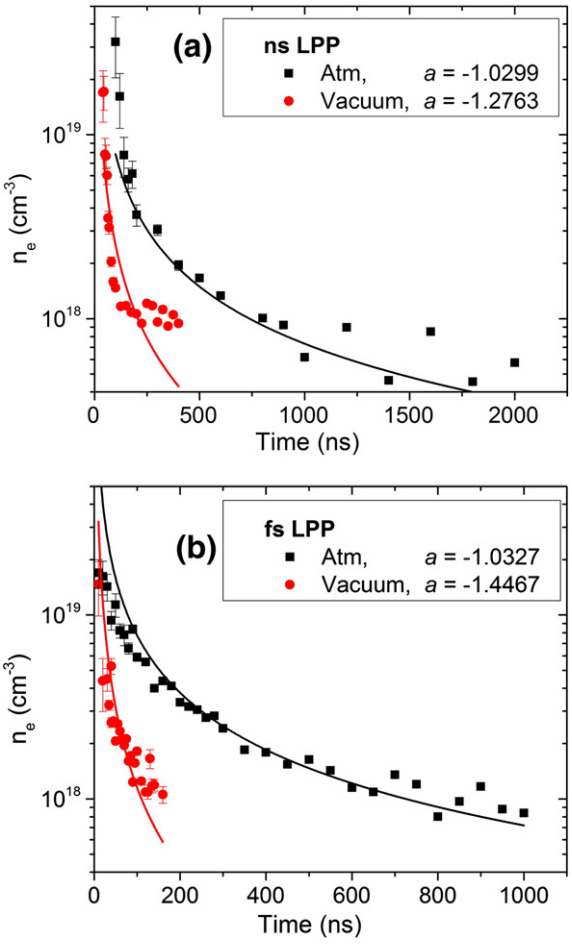

Fig. 5. Plasma electron density evolution with time after laser pulse for ns (a) and fs (b) LPP, fit with a power function. Exponential parameter of fitting function, a, provided in figure key. Electron density estimates made using Stark broadening technique and accounting for instrumental broadening. Error bars represent the confidence of the Lorentzian fitting function with the spectral line shape.

the excitation temperature can be determined from the slope of $\ln\left(\frac{I_{ki}\lambda}{g_k A_{ki}}\right)$ versus E_j, where I_{ki} is the intensity of the transition, λ is the wavelength of the transition, g_k is the degeneracy of the upper state, A_{ki} is the transition probability, k_B is the Boltzmann constant, T_{ex} is the excitation temperature, E_j is the energy of the upper state, h is Planck's constant, c is the speed of light, and $U(T_{ex})$ is the partition function [36,38]. Cu I spectral lines at 427.51 nm, 465.11 nm, 510.55 nm, 515.32 nm, and 521.82 nm were used for the Boltzmann plot. The validity of this method for temperature estimates hinges on the assumption of Local Thermal Equilibrium (LTE) within the plume. Assuming LTE implies that collisional processes, rather than radiative processes, are the dominant form of de-excitation and energy loss in the plasma and that temperature of the system determines the relative populations of excited levels of a species. This is referred to as the Atomic State Distribution Function and is described by the Boltzmann distribution [39–41]. The McWhirter criterion is often used to verify LTE conditions and justify temperature estimates using the Boltzmann plot method by establishing a minimum electron number density required to assume LTE [42]. The minimum electron density required to satisfy the McWhirter criterion has been estimated to be 10^{16} cm^{-3}. While this criterion can be fulfilled at a sufficient delay after the laser pulse, it is not sufficient to verify LTE because it is clear that the inhomogeneous, transient nature of LIBS plasmas does not fully satisfy LTE conditions and in these cases, results must be carefully considered [39].

Fig. 6 shows the decay of plasma excitation temperature in atmosphere and vacuum conditions for both ns and fs LPP. Integration times used were 10% of the gate delay after the laser pulse. The assumption of LTE to calculate temperature may not be valid at all times in plasma evolution, especially at earlier times after the laser pulse when the plasma is highly transient. This can be seen from the large error bars for those data point at short delays, where the Boltzmann plot fitting function returned large error values, though at later times when the assumption of at least partial LTE can be made, our Boltzmann plots showed high correlation values and error is significantly reduced. The presence of strong continuum emission caused by free electrons at early times of the plasma evolution, especially in the case of ns LPP where the laser pulse interacts with and ionizes the expanding plasma, also contributes to the large error at short delays and restricts reliable temperature estimates. Continuum emission was especially disruptive in atmosphere cases, where free electrons are confined by the ambient environment rather than expanding freely as in the vacuum case. Because neutral lines were used for determination of plasma temperature and density, sufficient populations of emitting neutral species must exist; the dominant mechanism for production of these neutral species being three-body recombination, the rate of which was given in Eq. (4). At early times in plasma evolution, neutral species populations are low for ns LPP compared to ionic species populations. This explains why temperature estimates at very early times were not possible and contributes towards the error in temperature seen at early times.

As was the case with electron density in Fig. 5, decay in temperature is seen to be more rapid in the case of vacuum environment for both ns and fs LPP, as the plume is able to expand freely to the point where insufficient emission can be collected from the probed volume. In the ambient air environment, sufficient emission to calculate temperature can be collected at significantly longer delays after the laser pulse because the ambient gas confines the plume, restricting expansion and increasing collision rates. Also of note and similar to the electron density results is the difference in time scales in Fig. 6(a) and (b). Expansion of the fs plume appears faster, reaching comparable temperatures to the ns plume in approximately half the time. Plume confinement also explains the higher temperatures in atmosphere compared to those in vacuum at identical delay times. Femtosecond LPP is expected to have significantly higher temperature than ns LPP at very early times due to a more than five order of magnitude difference in laser power caused by the shorter pulse width. This expected higher temperature is not seen because this

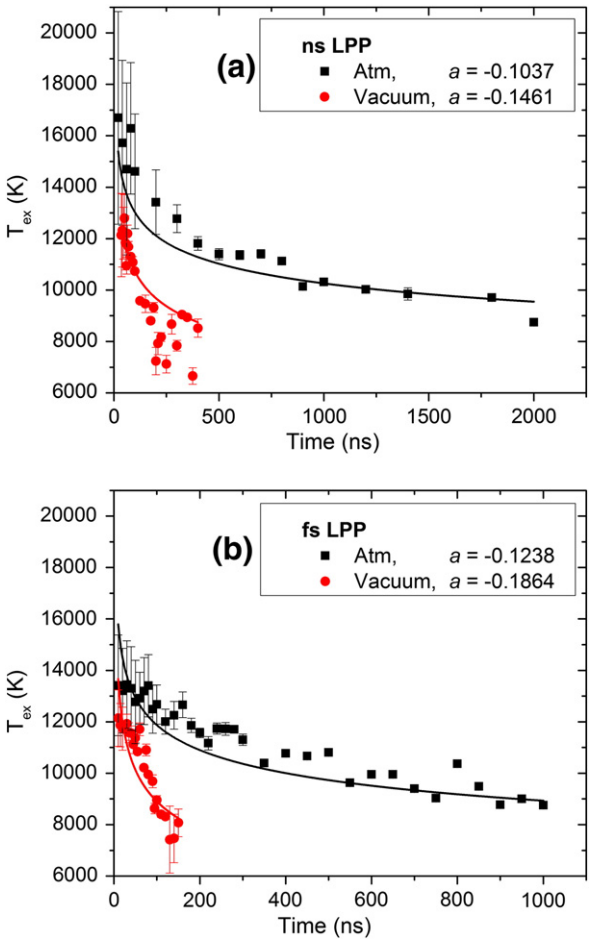

Fig. 6. Plasma excitation temperature evolution with time after laser pulse for ns (a) and fs (b) LPP, fit with a power function. Exponential parameter of fitting function, *a*, provided in figure key. Excitation temperature estimates made using Boltzmann plot method with error bars representing the confidence of the Boltzmann plot fitting function.

emission is from highly-charged ions emitting in the UV and X-ray regions. Ions produced from ns LPP are not expected to have as high charge states and hence, lower temperatures, though these lower-charged ions often emit in the visible region, as seen in Fig. 4.

Electron density and excitation temperature data shown in Figs. 5 and 6 were fitted with a power function of the form: $\psi(t) = ct^a$, where $\psi(t)$ represents electron density or excitation temperature as a function of time, t, c is a coefficient, and a is the exponential parameter defining the rate of decay. Values of the exponential parameter, a, for each plot, offering a numerical comparison of the decay of each plasma parameter, are provided in each figure key. To obtain an accurate comparison between exponential decay values, the coefficient of the power function, c, was fixed for both ns LPP and fs LPP data. We saw that fs LPP density and temperature decay more rapidly than for ns LPP. The differences in decay rates for fs LPP versus ns LPP of excitation temperature are shown to be more significant (20–30%) than those for electron density (0–15%). In the case of vacuum, we see more rapid decays due to free expansion and these differences between decay rates for ns LPP and fs LPP in vacuum are more pronounced than they are in atmosphere.

4. Conclusions

In this article we extended the work of our previous report [23] by investigating the dynamics of plasma evolution and characteristics of the emission spectra from ns and fs LPP during expansion into

vacuum and now atmosphere environments. Despite the significant difference in pulse durations from the two lasers, constant laser fluence was maintained to provide an accurate comparison and identify spectral characteristics and plasma dynamics produced by the vastly different ablation mechanisms of the two lasers.

ICCD images of plume emission were recorded. These images highlight the difference in expansion of ns and fs LPP. For both lasers, confinement by the ambient environment drastically limited plume expansion. While expansion of ns LPP displayed a wider angular distribution, appearing spherical in both environments, fs LPP expanded in a narrower angular distribution. This could be explained by the strong self-generated magnetic field created at early times during plasma expansion that pinches the expanding plume and influences its expansion in a direction normal to the target.

We also compared the spectral features from both LPP at different times after the laser pulse to see how the spectral shapes change with time and change with decreasing laser pulse width. It was observed that fs LPP emission spectra showed similar characteristics in both atmosphere and vacuum environments, while ns LPP emission spectra appeared to excite different ionic transitions in atmosphere and vacuum. In both environments, it was shown that continuum emission from ns LPP dominates at early times, while fs LPP demonstrated negligible continuum emission. Another important observation is that all ns LPP emission spectra showed transition lines from lower-charged ions, while fs LPP emission spectra were dominated only by neutral species emission. This can be explained by the different ablation processes for the two lasers, as ns lasers tend to generate lower-charged ion populations that through recombination, produce neutral species, while fs lasers create highly-charged ions emitting at much shorter wavelengths followed by thermal vaporization of the target, producing mostly neutral species. S/N and S/B ratios were calculated at different delays after the laser pulse to identify the importance of the delay time when collecting plasma emission for LIBS-related analysis.

Lastly, plasma excitation temperature and electron density were calculated using the Boltzmann plot and Stark broadening methods, respectively. These important plasma parameters are necessary to optimize a plasma emission source, as they are directly related to the emission characteristics of the plume species. It was shown that confinement by the ambient environment plays a significant role in maintaining plasma temperature and density and hence, emission at later times. This was the case for both ns and fs LPP, though ns LPP maintained these properties approximately two times longer than fs LPP, which can be attributed to the faster expansion of the fs plume. Power functions were fitted to this data to characterize the rapid decays seen in vacuum and to identify the more rapid decay exhibited by the fs LPP.

Acknowledgments

This work is supported by the US DOE National Nuclear Security Administration under award number DE-NA0001174.

References

[1] S.N. Thakur, J.P. Singh, Laser-Induced Breakdown Spectroscopy, 1st ed. Elsevier, Amsterdam. Boston, 2007.
[2] A.W. Miziolek, V. Palleschi, I. Schechter, Laser-Induced Breakdown Spectroscopy (LIBS): Fundamentals and Applications, Cambridge University Press, Cambridge, UK. New York, 2006.
[3] D.A. Cremers, L.J. Radziemski, Handbook of Laser-Induced Breakdown Spectroscopy, John Wiley & Sons, Chichester, West Sussex, England; Hoboken, NJ, 2006.
[4] A.P.M. Michel, M. Lawrence-Snyder, S.M. Angel, A.D. Chave, Laser-induced breakdown spectroscopy of bulk aqueous solutions at oceanic pressures: evaluation of key measurement parameters, Appl. Optics 46 (2007) 2507–2515.
[5] B. Salle, D.A. Cremers, S. Maurice, R.C. Wiens, P. Fichet, Evaluation of a compact spectrograph for in-situ and stand-off Laser-Induced Breakdown Spectroscopy analyses of geological samples on Mars missions, Spectrochim. Acta B 60 (2005) 805–815.
[6] D. Anglos, S. Couris, C. Fotakis, Laser diagnostics of painted artworks: Laser-induced breakdown spectroscopy in pigment identification, Appl. Spectrosc. 51 (1997) 1025–1030.
[7] J.L. Gottfried, F.C. De Lucia, C.A. Munson, A.W. Miziolek, Laser-induced breakdown spectroscopy for detection of explosives residues: a review of recent advances, challenges, and future prospects, Anal. Bioanal. Chem. 395 (2009) 283–300.
[8] S. Acquaviva, E. D'Anna, M.L. De Giorgi, F. Moro, Laser-induced breakdown spectroscopy for compositional analysis of multielemental thin films, Spectrochim. Acta Part B 61 (2006) 810–816.
[9] S. Almaviva, L. Caneve, F. Colao, R. Fantoni, G. Maddaluno, Laboratory feasibility study of fusion vessel inner wall chemical analysis by Laser Induced Breakdown Spectroscopy, Chem. Phys. 398 (2012) 228–232.
[10] S.G. Pavlov, S. Schroder, I. Rauschenbach, E.K. Jessberger, H.W. Hubers, Low-energy laser induced breakdown spectroscopy for in-situ space missions to solar system bodies without atmospheres, Planet. Space Sci. 71 (2012) 57–63.
[11] Y. Hirayama, M. Obara, Heat-affected zone and ablation rate of copper ablated with femtosecond laser, J. Appl. Phys. 97 (2005) 064903.
[12] I.U.A. Il'inskii, L.V. Keldysh, Electromagnetic Response of Material Media, Plenum Press, New York, 1994.
[13] A. Kaiser, B. Rethfeld, M. Vicanek, G. Simon, Microscopic processes in dielectrics under irradiation by subpicosecond laser pulses, Phys. Rev. B 61 (2000) 11437–11450.
[14] P.P. Pronko, P.A. VanRompay, C. Horvath, F. Loesel, T. Juhasz, X. Liu, G. Mourou, Avalanche ionization and dielectric breakdown in silicon with ultrafast laser pulses, Phys. Rev. B 58 (1998) 2387–2390.
[15] M.D. Perry, B.C. Stuart, P.S. Banks, M.D. Feit, V. Yanovsky, A.M. Rubenchik, Ultrashort-pulse laser machining of dielectric materials, J. Appl. Phys. 85 (1999) 6803–6810.
[16] R. Stoian, D. Ashkenasi, A. Rosenfeld, E.E.B. Campbell, Coulomb explosion in ultrashort pulsed laser ablation of Al2O3, Phys. Rev. B 62 (2000) 13167–13173.
[17] R.F.W. Herrmann, J. Gerlach, E.E.B. Campbell, Ultrashort pulse laser ablation of silicon: an MD simulation study, Appl. Phys. A: Mater. Sci. Process. 66 (1998) 35–42.
[18] E.L. Gurevich, R. Hergenroder, Femtosecond laser-induced breakdown spectroscopy: PHYSICS, applications, and perspectives, Appl. Spectrosc. 61 (2007) 233a–242a.
[19] W.-H. Tao, H.K. Yasuda, Measurement of spatial distributions of electron density and electron temperature in direct current glow discharge by double Langmuir probes, Plasma Chem. Plasma Process. 22 (2002) 297–311.
[20] H. Tojo, A. Ejiri, J. Hiratsuka, T. Yamaguchi, Y. Takase, K. Itami, T. Hatae, First measurement of electron temperature from signal ratios in a double-pass Thomson scattering system, Rev. Sci. Instrum. 83 (2012) 023507.
[21] W. Zhong, Z. Guixin, Z. Qing, J. Zhidong, A large-volume open-air microwave plasma based on parallel multislot rectangular waveguides, IEEE Trans. Plasma Sci. 40 (2012) 1380–1385.
[22] S.S. Harilal, C.V. Bindhu, R.C. Issac, V.P.N. Nampoori, C.P.G. Vallabhan, Electron density and temperature measurements in a laser produced carbon plasma, J. Appl. Phys. 82 (1997) 2140–2146.
[23] B. Verhoff, S.S. Harilal, J.R. Freeman, P.K. Diwakar, A. Hassanein, Dynamics of femto- and nanosecond laser ablation plumes investigated using optical emission spectroscopy, J. Appl. Phys. 112 (2012) 093303.
[24] R. Teghil, L. D'Alessio, A. Santagata, M. Zaccagnino, D. Ferro, D.J. Sordelet, Picosecond and femtosecond pulsed laser ablation and deposition of quasicrystals, Appl. Surf. Sci. 210 (2003) 307–317.
[25] B. Verhoff, S.S. Harilal, A. Hassanein, Angular emission of ions and mass deposition from femtosecond and nanosecond laser-produced plasmas, J. Appl. Phys. 111 (2012) 123304.
[26] T. Lehner, Intense self-generated magnetic field in the interaction of a femtosecond laser pulse with an underdense plasma, EPL (Europhys. Lett.) 50 (2000) 480.
[27] C. Thaury, P. Mora, A. Héron, J.C. Adam, Self-generation of megagauss magnetic fields during the expansion of a plasma, Phys. Rev. E 82 (2010) 016408.
[28] A.S. Sandhu, A.K. Dharmadhikari, P.P. Rajeev, G.R. Kumar, S. Sengupta, A. Das, P.K. Kaw, Laser-generated ultrashort multimegagauss magnetic pulses in plasmas, Phys. Rev. Lett. 89 (2002) 225002.
[29] Y.T. Li, J. Zhang, L.M. Cheng, J.F. Xia, H. Teng, Z.Y. Wei, W.M. Jiang, Observation of the transverse pinch of the expansion of an femtosecond laser-plasma, Acta Phys. Sin. 49 (2000) 1400–1403.
[30] Y.T. Li, J. Zhang, L.M. Chen, J.F. Xia, H. Teng, L.Z. Zhao, J.Q. Lin, Y.J. Li, Z.Y. Wei, L. Wang, W.M. Jiang, Optical diagnostics of femtosecond laser plasmas, Sci. China Ser. A-Math. Phys. Astron. 44 (2001) 98–102.
[31] L. Jiang, H. Tsai, Femtosecond laser ablation: challenges and opportunities, Proceeding of NSF Workshop on Research Needs in Thermal, Aspects of Material Removal, Stillwater, OK, Stillwater, OK, 2003, pp. 163–177.
[32] H.R. Griem, Principles of Plasma Spectroscopy, Cambridge University Press, Cambridge, Eng., New York, 1997.
[33] M.S. Dimitrijevic, S. Sahal-Brechot, Stark broadening of neutral zinc spectral lines, Astron. Astrophys. Suppl. 140 (1999) 193–196.
[34] D.W. Hahn, N. Omenetto, Laser-induced breakdown spectroscopy (LIBS), Part I: review of basic diagnostics and plasma–particle interactions: still-challenging issues within the analytical plasma community, Appl. Spectrosc. 64 (2010) 335a–366a.
[35] J.R. Freeman, S.S. Harilal, B. Verhoff, A. Hassanein, B. Rice, Laser wavelength dependence on angular emission dynamics of Nd: YAG laser-produced Sn plasmas, Plasma Sources Sci. Technol. 21 (2012) 055003.
[36] D.N. Patel, P.K. Pandey, R.K. Thareja, Stoichiometric investigations of laser-ablated brass plasma, Appl. Optics 51 (2012) B192–B200.
[37] M. Capitelli, A. Casavola, G. Colonna, A. De Giacomo, Laser-induced plasma expansion: theoretical and experimental aspects, Spectrochim. Acta B 59 (2004) 271–289.

[38] W. Lochte-Holtgreven, Plasma Diagnostics, Wiley, North-Holland, 1968.
[39] G. Cristoforetti, A. De Giacomo, M. Dell'Aglio, S. Legnaioli, E. Tognoni, V. Palleschi, N. Omenetto, Local thermodynamic equilibrium in laser-induced breakdown spectroscopy: beyond the McWhirter criterion, Spectrochim. Acta B 65 (2010) 86–95.
[40] H.R. Griem, Plasma Spectroscopy, McGraw-Hill, New York, 1964.
[41] T. Fujimoto, Plasma Spectroscopy, Clarendon Press; Oxford University Press, New York, Oxford, 2004.
[42] R.W.P. McWhirter, in: R.H. Huddlestone, S.L. Leonard (Eds.), Plasma Diagnostic Techniques, Academic Press, New York, 1965, pp. 201–264.